# A source model for the electron contamination of clinical linac heads in photon mode

**W. González, M. Anguiano, A. M. Lallena**

Departamento de Física Atómica, Molecular y Nuclear. Universidad de Granada. E-18071 Granada. Spain.

E-mail: wgonzalez@ugr.es,mangui@ugr.es,lallena@ugr.es

**Abstract.** In this work a general source model has been developed to describe the electron contamination in clinical linac heads when operating in photon mode. The model includes two-sources that take into account the electrons generated in the linac head and in the air gap between the linac head and the patient. Their geometrical characteristics are determined by fitting the model of total fluence distribution to a set of fluence data in air just before entering the water phantom and for various field sizes up to $40 \times 40\,\mathrm{cm}^2$. The electron energy distributions are fitted to those obtained from phase-space files calculated with PENELOPE at the patient surface and for the largest field size. To verify the model, percentage depth doses and transverse profiles in water obtained from a Monte Carlo simulation performed with a complete and detailed linac geometry are compared to those found with the source model. Six linacs (three operating at 6 MV, one at 15 MV and two at 18 MV) have been studied. A comparison with the results obtained with a single source model is also carried out. The two-source model proposed provides a reasonably good description of the dose absorbed in water for all irradiation fields considered. The largest differences occur at the entrance of the phantom, for the low energy configurations and the smaller fields, reaching $\sim 15\%$ at most. The two-source model describes much better than the single source one the lateral profiles in depth.

## 1. Introduction

It is commonly accepted that Monte Carlo (MC) simulation provides a rather accurate calculation tool to estimate the dose at the interface of heterogeneous tissues, regions where conventional algorithms suffer from inaccuracies (Chetty *et al* 2007). Different approaches can be followed to generate a source beam model. A straightforward procedure is to simulate the complete transport of the particles through all linac head elements and score a phase space file (PSF) at a convenient location such as the patient entrance. A PSF is a file that includes all details concerning all the particles arriving to the region of interest and it may be used as a source to calculate the dose distributions in the patient in a subsequent step. Though potentially accurate, this method has disadvantages as it requires a detailed knowledge of the geometry of the linac head

(including the materials conforming it), an information that is usually confidential and not available.

As an alternative, it is possible to develop analytical models in terms of several particle sources that describe the radiation entering the patient. These models should be reconstructed on the base of the information provided by experimental measurements performed on the specific linacs to be studied (Fippel *et al* 2003, Yang *et al* 2004, Sikora *et al* 2007). Usual source models considered in MC calculations for clinical photon beams include two photon sources and a third one that takes care of the electron contamination (Fippel *et al* 2003). The present work aims at developing a general model for the electron contamination source valid for any linac operating in photon mode.

Electron contamination significantly affects the dose absorbed at the entrance surface of patients and the first few millimeters in depth and therefore must be considered with enough accuracy. Ding (2002) studied in detail the spatial and energy behavior of photons and charged particles at the phantom surface for various field sizes and different photon beam energies. Their results show that at low energies (6 MV) and for large field sizes of $40\,\mathrm{cm} \times 40\,\mathrm{cm}$, the dose due to electron contamination can be up to 20% of the total doses deposited at the surface and this percentage is even larger, of the order of 30% for higher energies. Also, it has been observed that dose tolerance limits in skin may be exceeded in intensity modulated radiotherapy treatments if electron contamination is ignored (Lee *et al* 2009).

Different electron contamination virtual source models (VSM) have been considered in both analytical and MC algorithms for dose calculations. Almost all electron contamination VSMs that can be found elsewhere follow Gaussian spatial distributions. Ahnesjö *et al* (1992) showed that contaminant charged particle fluence at the patient surface are to a good approximation of Gaussian type. Yang *et al* (2004) checked this conclusion by analyzing a PSF scored above the secondary collimators of a Siemens Primus linac operating at 6, 10 and 18 MV; they found that contaminant electrons are distributed with a Gaussian shape and an amplitude which depends on the field size. Sikora and Alber (2009), following a similar procedure, found that the Gaussian distributions required must include a dependence on the energy. According to Ulmer *et al* (2005) the electron contamination fluence is strongly dependent on the position of the jaws and can be modeled using a Gaussian-like source plus a correction kernel for small irradiation fields. Korhonen (2009) used a combination of two Gaussian sources to model the small fields with enough accuracy. On the experimental side, the results obtained by Ding (2002) and López-Medina *et al* (2005) indicate that the electrons produced in air have a significant contribution.

In this work we propose a two-source model and study its capabilities in the case of three linacs: an Elekta Precise (Elekta Group, Crawly, UK), with qualities of 6 and 15 MV, and a Varian Clinac 2300C/D (Varian Medical System, Palo Alto, CA) and a Siemens Mevatron KDS (Siemens Medical Systems, Oncology Care Systems, Concord, USA), both with qualities 6 and 18 MV. The results obtained with the VSM have been compared to those found in complete simulations of these linacs in which their detailed

geometry is considered. Also a comparison with a single source model similar to that of Sikora and Alber (2009) is carried out.

## 2. Material and methods

### *2.1. Details of the Monte Carlo simulations*

In this work the six beams produced by the three linacs of clinical above mentioned have been simulated. The corresponding geometries have been constructed according to the information provided by the manufacturers. Table 1 shows some of the characteristics relevant for the simulations performed. Monoenergetic electron beams, with an initial energy $E_e^{\rm ini}$ and spatially distributed according to a Gaussian distribution with a full width at half-maximum $\mathrm{FWHM}_e^{\rm ini}$, are made to scatter onto the target. The values for the 6 MV Precise are those used in a previous work in which the linac was matched with measurements and the dosimetric characteristics of a micro-multileaf collimator were analyzed (González *et al* 2011). For the 6 and 18 MV Clinac configurations, as well as for the 15 MV Precise, the values are those provided by default in PRIMO, a MC based treatment planning system (Rodríguez *et al* 2013). Finally, the parameters for the two Mevatron configurations are the same as those considered in the work of Sheikh-Bagheri and Rogers (2002).

In the three linacs, the collimation system consists of two pair of jaws. The upper jaws are in the $y$-direction while the lower ones move in the $x$ one. The Precise linac includes, in addition, a multileaf collimator above the upper jaws; in our simulations it has been considered as an additional $y$-pair of jaws (details can be found in González *et al* 2011.)

The MC code PENELOPE (version 2008) was used to perform the simulations (Salvat *et al* 2008). The code describes the coupled transport of photons, electrons and positrons in any material and geometry. The simulation is controlled by the parameters C1, C2,

**Table 1.** Values of the energy and the FWHM of the spatial distribution of the electrons incident on the linac target used in the MC simulations carried out. The position of the scatter source, $z_{\rm S}$, as well as the upstream, $z_{\rm U}^x$ and $z_{\rm U}^y$, and downstream, $z_{\rm D}^x$ and $z_{\rm D}^y$, limits of the collimation system in the transverse directions for the linacs studied are also given. These $z$-values are relative to the upper plane of the photon target to which we assign $z = 0$.

| linac | quality (MV) | $E_e^{\rm ini}$ (MeV) | $\mathrm{FWHM}_e^{\rm ini}$ (mm) | $z_{\rm S}$ (cm) | $z_{\rm U}^x$ (cm) | $z_{\rm D}^x$ (cm) | $z_{\rm U}^y$ (cm) | $z_{\rm D}^y$ (cm) |
|---|---|---|---|---|---|---|---|---|
| Precise | 6 | 6.3 | 1.2 | 15.8 | 43.1 | 50.9 | 29.8 | 42.6 |
| | 15 | 16.0 | 1.4 | | | | | |
| Clinac | 6 | 6.3 | 1.3 | 12.8 | 36.7 | 44.5 | 28.0 | 35.8 |
| | 18 | 20.7 | 3.0 | | | | | |
| Mevatron | 6 | 6.8 | 3.2 | 10.0 | 30.3 | 37.8 | 22.5 | 30.0 |
| | 18 | 14.7 | 1.0 | | | | | |

**Table 2.** Simulation parameters for the various materials used in the linac geometries.

| Material | C1 | C2 | WCC (keV) | WCR (keV) | EABS($\gamma$) (keV) | EABS($e^-$) (keV) | EABS($e^+$) (keV) |
|---|---|---|---|---|---|---|---|
| Cu | 0.2 | 0.2 | 10.0 | 1.0 | 100.0 | 10.0 | 10.0 |
| Al, Graphite, Ti | 0.1 | 0.1 | 10.0 | 1.0 | 10.0 | 1.0 | 1.0 |
| Be, Fe, Ta | 0.1 | 0.1 | 10.0 | 1.0 | 10.0 | 1.0 | 10.0 |
| Air | 0.05 | 0.05 | 1.0 | 0.1 | 1.0 | 0.1 | 0.1 |
| Water | 0.02 | 0.02 | 1.0 | 0.1 | 1.0 | 0.1 | 0.1 |
| W (collimators) | 0.15 | 0.15 | 10.0 | 1.0 | 10.0 | 1.0 | 1.0 |
| Au, Steel, W (target) | 0.01 | 0.01 | 1.0 | 0.1 | 1.0 | 0.1 | 0.1 |

WCC, WCR, EABS($\gamma$), EABS($e^-$) and EABS($e^+$) that must be chosen for each material in the geometry. The values used in our simulations for these parameters are given in table 2. All details about the code and the tracking parameters can be found in the PENELOPE user manual (Salvat *et al* 2008).

To determine some of the characteristics of the source model, some PSFs scored at given planes, for the largest radiation field of each linac, in complete MC simulations (including the detailed linac head geometries) have been used. In particular we have calculated the $\mathrm{PSF_{sc}}$, just above the whole secondary collimation system, and the $\mathrm{PSF_{ph}}$ at the entrance of a water phantom, at 100 cm from the source, that mimics the patient.

### *2.2. Spatial distributions of the electron sources*

We propose a model that involves two electron sources. It is formally similar to the photon VSM of Fippel *et al* (2003). The first one describes the electrons produced in the various elements of the linac head and it is situated just below the flattening filter of the linac, at $z_{\mathrm{S}}$. The second electron source takes into account the contribution of the electrons produced in the air gap between the linac and the patient. In our model we have situated it at $z_{\mathrm{U}}^{y}$, above the secondary collimator of the linac. Table 1 shows the values of these positions for all three linacs studied.

In our model we assume that the total electron fluence at a point $(x, y, z)$ is

$$\phi_{\mathrm{e}}(x,y,z) \;=\; w_{\mathrm{H}}\,\phi_{\mathrm{H}}(x,y,z)\,\phi^{\mathrm{e}}_{\mathrm{horn}}(x,y,z) \;+\; w_{\mathrm{A}}\,\phi_{\mathrm{A}}(x,y,z)\,, \tag{1}$$

where $\phi_{\mathrm{H}}(x,y,z)$ is the fluence due to the electrons produced in the linac head and $\phi_{\mathrm{A}}(x,y,z)$ is that corresponding to the electrons produced in-air. Here $w_{\mathrm{H}}$ and $w_{\mathrm{A}}$ represent the relative weights of the two-sources and verify

$$w_{\mathrm{H}} \;+\; w_{\mathrm{A}} \;=\; 1\,. \tag{2}$$

The function

$$\phi^{\mathrm{e}}_{\mathrm{horn}}(x,y,z) \;\equiv\; \phi^{\mathrm{e}}_{\mathrm{horn}}(\rho) \;=\; 1 \;+\; \rho^2 \sum_{j=0}^{4} f_j\,\rho^j \tag{3}$$

is a correction dependent on $\rho = \sqrt{x^2+y^2}/(z-z_{\rm S})$, that is introduced to take into account possible variations between the center and the edges of the flat region of the radiation field, thus making the model more flexible to describe transverse profiles.

Both the head and the air sources are supposed to follow a distribution of the form:

$$S_\alpha^{\rm G}(x,y) \,=\, G_{\sigma_\alpha}(x)\, G_{\sigma_\alpha}(y)\,, \quad \alpha \,=\, {\rm H, A}\,, \tag{4}$$

with

$$G_{\sigma_\alpha}(t) \,=\, \frac{1}{\sqrt{2\pi}\,\sigma_\alpha}\,\exp\left(-\frac{t^2}{2\,{\sigma_\alpha}^2}\right) \tag{5}$$

a Gaussian function. The corresponding fluence contribution is given by

$$\phi_\alpha^{\rm G}(x,y,z) \,=\, \frac{(z_{\rm D}^x - z_\alpha)(z_{\rm D}^y - z_\alpha)}{(z-z_\alpha)^2}\, I_\alpha\,, \tag{6}$$

where

$$I_\alpha \,=\, \int_{-x_\alpha^-}^{x_\alpha^+}\int_{-y_\alpha^-}^{y_\alpha^+} {\rm d}x'\,{\rm d}y'\, S_\alpha(x',y')\,, \tag{7}$$

with the integration limits $x_\alpha^\pm$ and $y_\alpha^\pm$ given in the Appendix below. For the Gaussian-like function $S_\alpha$, the integrals can be calculated analytically resulting

$$I_\alpha \,=\, \frac{1}{4}\,\left[{\rm erf}\left(\frac{\tilde{x}_\alpha^+}{\sigma_\alpha}\right) + {\rm erf}\left(\frac{\tilde{x}_\alpha^-}{\sigma_\alpha}\right)\right]\,\left[{\rm erf}\left(\frac{\tilde{y}_\alpha^+}{\sigma_\alpha}\right) + {\rm erf}\left(\frac{\tilde{y}_\alpha^-}{\sigma_\alpha}\right)\right]\,, \tag{8}$$

where erf refers to the well-known error function, $\tilde{x}_\alpha^\pm = x_\alpha^\pm/\sqrt{2}$ and $\tilde{y}_\alpha^\pm = y_\alpha^\pm/\sqrt{2}$.

The parameters of the sources were determined by using the Levenberg-Marquardt minimization method (Press *et al* 1992), making the fluence in equation (1) to fit a series of fluence profiles calculated in air in a complete MC simulation including the detailed linac geometries. Specifically, we extracted from the $\rm PSF_{ph}$, that is at 100 cm from the source, electron fluence profiles in the $x$ (with $y=0$) and $y$ (with $x=0$) directions determined for radiation fields with sizes $2\times2$, $3\times3$, $5\times5$, $10\times10$, $20\times20$, $40\times40$, $5\times40$, $10\times40$, $40\times5$ and $40\times10$ cm$^2$. In the case of the Mevatron the maximum aperture is 35 cm instead of 40 cm. In the simulations performed to generate these fluence profiles, the specular symmetry shown by the jaws was taken into account. All fluence distributions were normalized to the value of the fluence at the point $(0,0,100\,{\rm cm})$, for the maximum squared field.

As indicated above, we have compared this two-source model to that proposed by Sikora and Alber (2009) in which a single source situated just below the flattening filter, at $z_{\rm S}$, is considered. The spatial distribution is of Gaussian type with a width that depends on the energy:

$$p_{\rm e}^{\rm SA}(r;\sigma(E)) \,=\, N_r^{\rm SA}\,\frac{1}{\sqrt{2\pi}\,\sigma(E)}\,\exp\left[-\frac{r^2}{2\sigma^2(E)}\right]\,, \tag{9}$$

where

$$\sigma(E) \,=\, (E/{\rm MeV})^k\,\sigma_{\rm ref}\,. \tag{10}$$

The values of the parameters $\sigma_{\rm ref}$ and $k$ are determined for each linac configuration in the following way. First, the electrons in $\mathrm{PSF_{sc}}$ not hitting the secondary collimators in the case of the largest radiation field are moved back to the $z_{\rm S}$ plane, according to the direction of movement they have when they reach the $\mathrm{PSF_{sc}}$ scoring plane. The function $p_{\rm e}^{\rm SA}(r;\sigma(E))$ in equation (9) is then fitted to the electron distribution obtained. In this manner the electrons produced in the air gap between the flattening filter and the secondary collimators are automatically taken into account.

### *2.3. Energy spectra of the electron sources*

In the source models proposed by Fippel *et al* (2003) and Sikora and Alber (2009) the energy distribution of the electron contamination source is given in terms of a decaying exponential. Alternatively, Yang *et al* (2004) considered a log-normal distribution, similar to that used for the photon sources. In the present work we have studied two different distributions. The first one is similar to that proposed by Yang *et al* (2004):

$$p_{\rm e}^{\rm Y}(E) \;=\; N_{\rm e}^{\rm Y}\,\frac{1}{\sqrt{2\pi}\,(E/{\rm MeV})\,\sigma_{\rm e}}\,\exp\left\{-\frac{[\log(E/{\rm MeV})-\mu_{\rm e}]^2}{2\,\sigma_{\rm e}^2}\right\}\,, \qquad (11)$$

that includes three free parameters, $N_{\rm e}^{\rm Y}$, $\mu_{\rm e}$ and $\sigma_{\rm e}$. We have also considered a second function which is a modification of a distribution proposed by Ulmer et al. (2005) and Sikora et al. (2007) for a photon VSM:

$$p_{\rm e}^{\rm G}(E) \;=\; N_{\rm e}^{\rm G}\,\frac{\exp\left[b_{\rm e}\,(E_e^{\rm max}-E)/{\rm MeV})\right]\,-\,1}{\exp(b_{\rm e}\,E_e^{\rm max}/{\rm MeV})}\,\left\{1\,-\,\exp\left[-s_{\rm e}\,(E-E_e^{\rm min})/{\rm MeV}\right]\right\}\,. \qquad (12)$$

It has three free parameters, $N_{\rm e}^{\rm G}$, $b_{\rm e}$ and $s_{\rm e}$. The energies $E_e^{\rm max}$ and $E_e^{\rm min}$ in this equation are, respectively, the maximum and minimum energies of the electrons in $\mathrm{PSF_{ph}}$.

To determine the values of the free parameters, these two distributions were fitted to the energy spectra of the electrons scored in the $\mathrm{PSF_{ph}}$ at the entrance of the water phantom. For that purpose the Levenberg-Marquardt minimization method (Press *et al* 1992) was used and the Akaike information criterion (Akaike 1974) was applied to choose among the two distributions.

### *2.4. Evaluation of the source model*

In order to evaluate the model proposed, a comparison of absorbed dose distributions in the water phantom obtained with our source model and using the "pseudo-data" provided by the PENELOPE simulation with the complete linac geometry was done. The simulations performed for the source model were carried out with the MC code DPM (Sempau *et al* 2000), a dedicated code for applications in medical physics problems. The comparison was done for percentage depth doses and transverse profiles at various depths, both in- and off-axis of the beam, in a $50\times50\times40$ cm$^3$ water phantom situated with source-to-surface distances of 100 and 115 cm. Squared radiation fields of $5\times5$, $10\times10$ and $20\times20$ cm$^2$ defined at the water surface were considered. Also a half

beam field (that is, not centered with respect to the beam axis) of $5 \times 10\,\mathrm{cm}^2$ was also analyzed.

In the simulations performed with the two-source model we propose in the present work, the initial particles were generated according to the following procedure:

(i) First it is chosen which one of the two-sources emits the initial electron. This is done by using the weights $w_{\mathrm{H}}$ and $w_{\mathrm{A}}$ defining the relative weight of the two fluences in the total electron fluence (see equation (1)). At this step, the $z$-coordinate of the initial electron is determined being either $z_{\mathrm{S}}$, for the head source, or $z_{\mathrm{U}}^{y}$, for the in-air one.

(ii) The next step consists in determining the position of the initial electron $(x, y)$ at the source plane. This is done by sampling the corresponding distribution $S_{\alpha}^{\mathrm{G}}(x, y)$ (see equation (4)).

(iii) After this, the emission direction of the initial electron must be fix. If the electron is emitted from the head source, the distribution functions $\phi_{\mathrm{horn}}^{\mathrm{e}}(x, y = 0, z = z_{\mathrm{sample}})$ and $\phi_{\mathrm{horn}}^{\mathrm{e}}(x = 0, y, z = z_{\mathrm{sample}})$, with $z_{\mathrm{sample}} = (z_{\mathrm{D}}^{x} + z_{\mathrm{D}}^{y})/2$, are sampled to obtain a pair $(x, y)$. In the case the electron is emitted from the air source a similar procedure is followed but in that case uniform distributions are sampled within the field defined by the collimator system at the water phantom entrance. The coordinates $x$ and $y$ determined in this way together with those of the initial position of the electron emitted (determined in the previous step) define the emission direction.

(iv) Finally, the initial electron energy is sampled from the energy distribution $p_e^{\mathrm{G}}$ (see equation (12)) that is being considered. As shown below this distribution provides a better description of the electron spectra than $p_e^{\mathrm{Y}}$ (see equation (11)) and that is why we have considered it in the evaluation simulations.

As indicated above, the results obtained with this model have been compared to those found using a single source model similar to that of Sikora and Alber (2009). In the simulations developed with this last model the initial electrons were generated as follows:

(i) First the initial energy $E$ is obtained by sampling the energy distribution $p_e^{\mathrm{G}}$.

(ii) Then the $\sigma(E)$ of the spatial distribution is calculated according to equation (10).

(iii) After this, the spatial distribution $p_e^{\mathrm{SA}}$, given in equation (9), is sampled to fix a value of $r$. The initial position of the emitted electron $(x, y)$ is determined uniformly in the circumference of radius $r$. We remember that the $z$ initial position in this case is $z_{\mathrm{S}}$.

(iv) To obtain the emission direction one samples uniformly the field size at the water phantom entrance to calculate a pair $(x, y)$ that, together with the initial position determined in the previous step define the emission direction of the electron.

After generating all characteristics (position, emission direction and energy) of the primary electron, it is transported using the DPM code and the dose absorbed in the

water phantom is calculated. In these simulations the voxels used to score the energy deposited in water have dimensions of 0.8 cm × 0.8 cm × 0.2 cm. Same scoring voxels were used in the complete simulations with PENELOPE that were carried out with the same $PSF_{ph}$ considered to calculate the fluence profiles fitted with the proposed VSM. The CPU times ranged between 40 min, for the 5 cm × 5 cm field, and 130.0 min, for the 20 cm × 20 cm. The DPM calculations for the VSM required between 0.6 min and 2.2 min and the number of electron histories considered was $10^7$. The statistical uncertainties of these calculations were below 2% (with a coverage factor $k = 1$). For the comparison, the dose distributions obtained were normalized to the value in the beam axis at $z_{ref} = 0.5$ cm, for 6 MV, and $z_{ref} = 1.1$ cm, for 15 and 18 MV.

## 3. Results and discussion

### *3.1. Fluence distributions*

First the electron fluence given by equation (1) was fitted to the "pseudo-data" obtained from the complete MC simulation. The values of the best fit parameters are shown in table 3. Some of the fits obtained are plotted in figure 1 where the MC results (symbols) and the fitted electron fluences (solid curves) are shown. Similar results are obtained for all the radiation field used in the fitting procedure. In general the fluences are rather well described by using the two-source model proposed.

The weights $w_H$ of the head source are larger for the higher energy operation modes. Figure 2 shows the contributions to the total fluence of the two sources for the two Clinac configurations. The results obtained for the 10 cm × 10 cm and 40 cm × 40 cm radiation fields are shown. In the first case (upper panels) the head source (dotted curve) dominates the fluence, independently of the linac configuration. In the case of the largest field size the relative importance of the two sources changes from the 6 MV mode, where the in-air head dominates, to the 18 MV one, for which the head source gives the biggest contribution to the total fluence. These results show an overall agreement with the findings of Ding (2002), except for the 10 cm × 10 cm field at 6

**Table 3.** Parameters of the electron sources obtained after fitting the fluence data with the function $\phi_e$ given in equation (1). Uncertainties with a coverage factor $k = 1$ are given between parentheses; that is, 19.6(5) means $19.6 \pm 0.5$.

| linac | quality (MV) | $w_H$ | $\sigma_H$ (mm) | $\sigma_A$ (mm) |
|---|---|---|---|---|
| Precise | 6 | 0.20(6) | 16.6(6) | 33.9(5) |
| | 15 | 0.67(9) | 25.4(5) | 30.8(6) |
| Clinac | 6 | 0.30(6) | 19.6(5) | 34.0(5) |
| | 18 | 0.74(3) | 30.4(6) | 37.1(5) |
| Mevatron | 6 | 0.26(2) | 11.9(5) | 26.8(6) |
| | 18 | 0.73(3) | 24.2(6) | 29.4(5) |

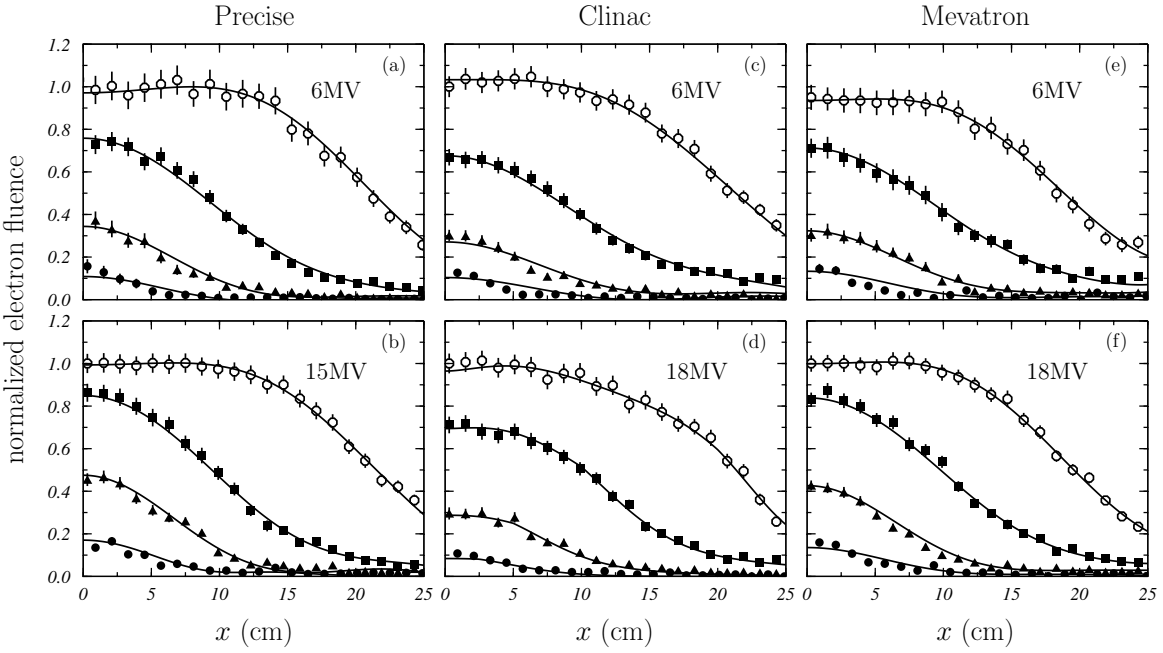


**Figure 1.** Electron fluences at $z = 100\,\mathrm{cm}$, normalized to the maximum fluence of the largest field size. Results for the six configurations studied are shown. Symbols represent the results from the complete MC simulation: $5\,\mathrm{cm} \times 5\,\mathrm{cm}$ (circles), $10\,\mathrm{cm} \times 10\,\mathrm{cm}$ (triangles), $20\,\mathrm{cm} \times 20\,\mathrm{cm}$ (squares) and $40\,\mathrm{cm} \times 40\,\mathrm{cm}$ (open circles). Solid curves represent the fits using equation (1) for $\phi_\mathrm{e}$.

MV. In this last case, he found that the electrons produced in the air gap between the linac head and the phantom are $\sim 70\%$ of the total amount of contaminant electrons. The discrepancy may be due to the fact that Ding obtained his results from a detailed analysis of the PSF at the phantom entrance, while ours come from a fitting procedure.

Korhonen (2009) studied several linacs other than those here analyzed. She modeled the electron energy fluence as a convolution of the energy fluence due to primary photons with a dual Gaussian kernel, thus allowing an accurate description of the field size dependence of the electron contamination. She obtained weights of 0.22 for a 6 MV Elekta SL, 0.31 for a 6 MV Varian 2100 C/D and 0.26 for a 6 MV Siemens Primus, values all of them very close to those we have found, despite the differences in the linac geometries. For the linacs operating at higher energies, the weights found by Korhonen ranged between 0.46 and 0.54, smaller than those obtained in our fitting procedure.

The head source is smaller for the low energies, being $12 - 20\,\mathrm{mm}$ for 6 MV and $24 - 30\,\mathrm{mm}$ for the high energy qualities. The in-air source size is relatively independent of the linac quality though it is always bigger than the head source size. This is mainly due to the fact that those electrons coming from the head and having large scatter angles will be strongly attenuated by the secondary collimators and the model does not account for them. The same behavior can be observed in the results obtained by Korhonen (2009).

In figure 3 we show with solid, dotted and dashed lines the functions $\phi^\mathrm{e}_\mathrm{horn}$, given in

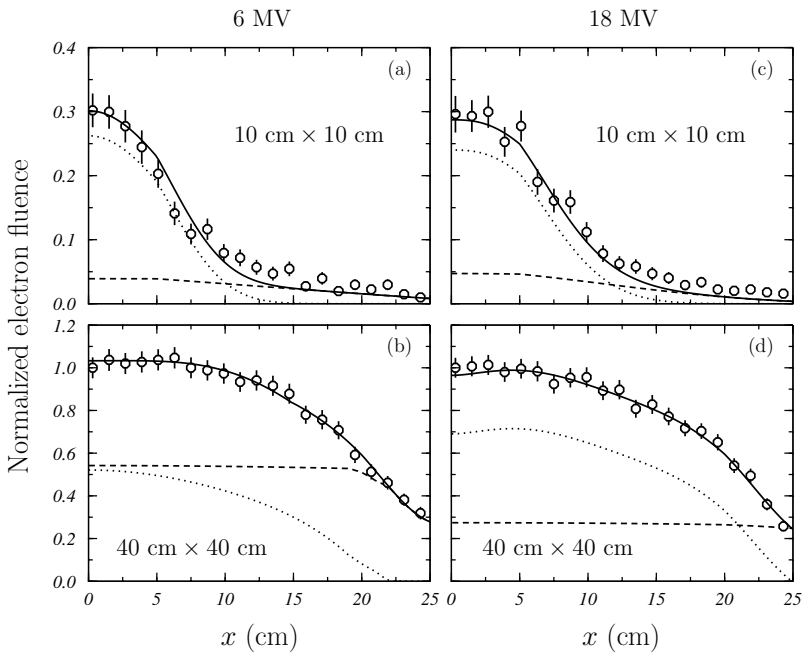


**Figure 2.** Electron fluences at $z = 100\,\mathrm{cm}$, normalized to the maximum fluence of the largest field size, for the 6 MV (left panels) and 18 MV (right panels) Clinac configurations. Upper panels correspond to $10\,\mathrm{cm} \times 10\,\mathrm{cm}$ field while lower panels are for $40\,\mathrm{cm} \times 40\,\mathrm{cm}$. Symbols represent the result obtained in the MC simulations including the complete linac geometries. Solid curves are the fitted fluences. Dotted and dashed curves are the fluences corresponding to the head and the in-air sources.

equation (3) and obtained in the fitting procedure for the Precise, Clinac and Mevatron KDS linacs studied at $z = 100\,\mathrm{cm}$. The results for low (high) energy configurations are plotted in the upper (lower) panel. As it can be seen, $\phi^{\mathrm{e}}_{\mathrm{horn}}$ depends essentially on the nominal energy of the linac configuration. For 6 MV, it remains constant, equals to 1, up to $\sim 5\,\mathrm{cm}$.

### *3.2. Energy spectra*

In figure 4 the electron energy spectra obtained from the $\mathrm{PSF}_{\mathrm{ph}}$ for the largest radiation field is shown with solids circles. An analysis of the spectra obtained for smaller radiation fields did not show up significant differences. The energy distributions $p^{\mathrm{Y}}_{\mathrm{e}}$, defined in equation (11), and $p^{\mathrm{G}}_{\mathrm{e}}$, given in equation (12) were fitted to these data and the results are shown with dashed and solid curves, respectively. Table 4 shows the values of the fitting parameters. In general, the fits provided by both distributions are rather similar. In fact, the values of the Akaike's criterion parameter $a$ (see table) obtained for both models are close to each other, though they are larger in absolute value for $p^{\mathrm{G}}_{\mathrm{e}}$. Even more, as seen in the figure the $p^{\mathrm{Y}}_{e}$ fitted distributions show an extremely long tail at large energies and their sampling in actual simulations could generate electrons with energies unrealistically large. As a consequence we have chose $p^{\mathrm{G}}_{e}$ to describe the energy spectra of the initial electrons.

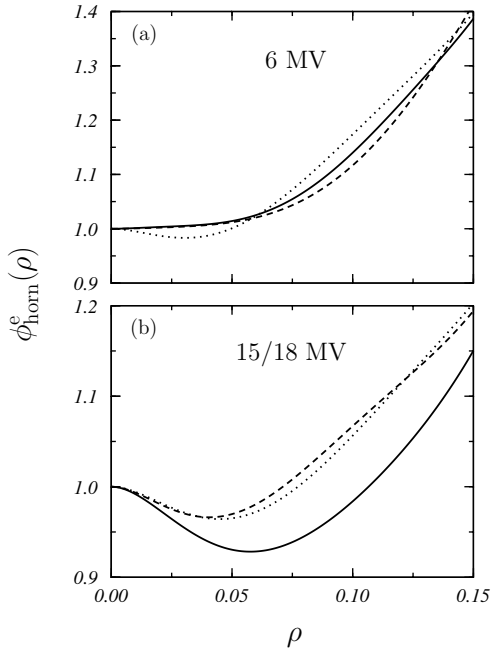


**Figure 3.** Functions $\phi^{\rm e}_{\rm horn}$, as given by equation (3), obtained in the fits performed using $\phi_{\rm e}$. The plots correspond to $z = 100$ cm. The results for the three linacs operating at 6 MV are shown in panel (a) while those corresponding to higher energies are in panel (b). Solid, dotted and dashed curves correspond to the Precise, Clinac and Mevatron KDS linacs, respectively.

In the case of the Precise (panels (a) and (b)) we have also included, with open squares, the results quoted by Sikora and Alber (2009) coveniently normalized. As seen they show the same trend as that found in our simulations.

**Table 4.** Values of the parameters of the distributions $p_{\rm e}^{\rm Y}$ and $p_{\rm e}^{\rm G}$, as defined in equations (11) and (12), respectively, obtained after the fit to the corresponding spectra shown in figure 4.

| | | $p_{\rm e}^{\rm Y}$ | | | | $p_{\rm e}^{\rm G}$ | | | |
|---|---|---|---|---|---|---|---|---|---|
| linac | quality (MV) | $N_{\rm Y}$ (MeV$^{-1}$) | $\mu_{\rm e}$ | $\sigma_{\rm e}$ | $a$ ($\times 10^{-3}$) | $N_{\rm e}$ (MeV$^{-1}$) | $b_{\rm e}$ | $s_{\rm e}$ | $a$ ($\times 10^{-3}$) |
| Precise | 6 | 0.11(1) | 1.20(5) | 1.02(3) | −0.5 | 0.08(1) | 0.60(1) | 24.9(4) | −0.6 |
| | 15 | 0.11(1) | 2.26(7) | 1.21(2) | −1.5 | 0.04(1) | 0.36(1) | 21.4(1) | −1.8 |
| Clinac | 6 | 0.10(1) | 1.00(5) | 0.98(4) | −0.5 | 0.09(1) | 0.77(1) | 40.0(7) | −0.7 |
| | 18 | 0.11(1) | 3.11(9) | 1.30(3) | −2.1 | 0.03(1) | 0.27(1) | 24.0(8) | −2.5 |
| Mevatron | 6 | 0.10(1) | 0.95(4) | 0.97(3) | −0.5 | 0.09(1) | 0.82(1) | 36.4(8) | −0.7 |
| | 18 | 0.11(1) | 2.95(8) | 1.25(2) | −1.4 | 0.03(1) | 0.31(1) | 29.1(7) | −1.7 |

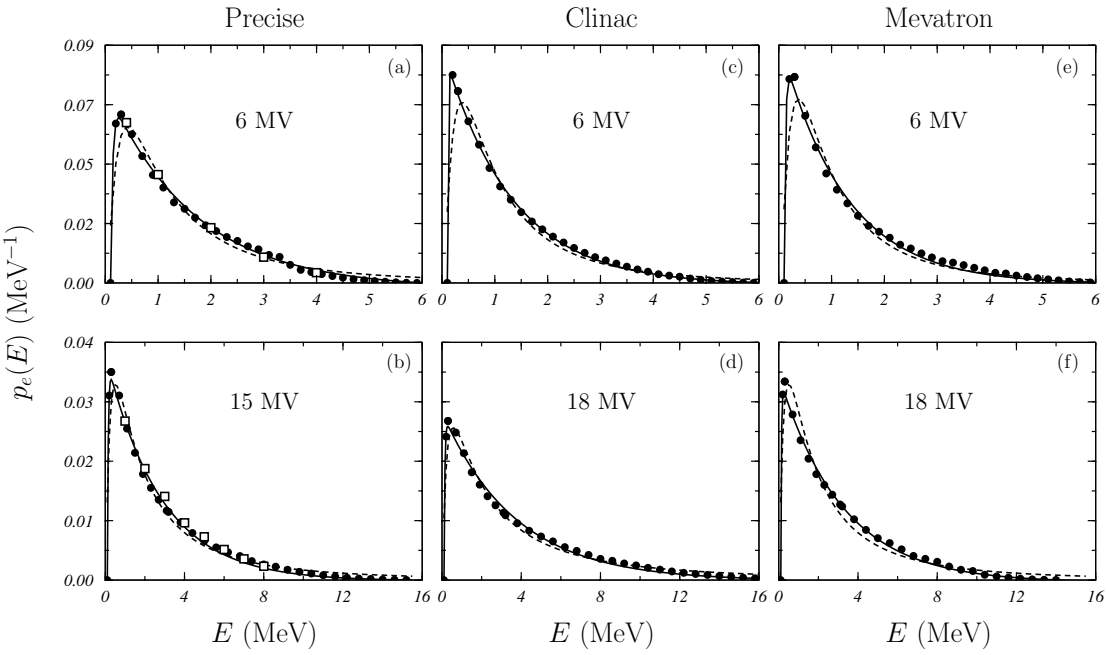


**Figure 4.** Energy spectra for the largest radiation field at 100 cm. Solid circles have been obtained from the $\mathrm{PSF_{ph}}$ calculated for each linac. Dashed and solid curves are the best fits found for the distributions $p_e^{\mathrm{Y}}$ and $p_e^{\mathrm{G}}$, defined in equations (11) and (12), respectively. Open squares are the results quoted by Sikora and Alber (2009) renormalized to the maximum of our curves. Uncertainties are given with a coverage factor $k = 1$.

### *3.3. Comparing the models*

Once the source model was established, it was evaluated by comparing percentage depth doses and transverse profiles at different depths in the water phantom (with a source-to-surface distance of 100 cm) calculated with the VSM (using DPM) with those obtained within a complete simulation with PENELOPE. In- and off-axis profiles were considered for various field sizes.

Figures 5 and 6 show those comparisons for the Precise at 6 MV and the Clinac at 18 MV. Similar results are obtained for the other linac configurations. The results obtained by the PENELOPE calculation are represented with symbols while solid lines correspond to those given by the two-source model with DPM. In general the VSM provides a rather good description of the PENELOPE "pseudo-data" in all cases analyzed. The largest differences ($\sim 15\%$) are found at the entrance of the phantom and for the low energy configurations and the smaller radiation fields (see *e. g.*, figure 5 panels (a) y (c)). The reasons of these differences are not clear and would require a more detailed study.

Figures 5 and 6 also include (see dashed lines) the results obtained with the single-source model described above. Table 5 shows the values of the parameters $\sigma_{\mathrm{ref}}$ and $k$ obtained in the fitting of the distribution $p_{\mathrm{e}}^{\mathrm{SA}}(r;\sigma(E))$. Both parameters are similar for the two qualities analyzed in each linac though the values found for the Mevatron are

**Table 5.** Values of the fitting parameters of $p_{\rm e}^{\rm SA}(r;\sigma(E))$ as given in equations (9)-(10). Uncertainties with a coverage factor $k = 1$ are given between parentheses; that is, 33.8(5) means $33.8 \pm 0.5$.

| linac | quality (MV) | $\sigma_{\rm ref}$ (mm) | $k$ |
|---|---|---|---|
| Precise | 6 | 31.8(4) | −0.16(1) |
| | 15 | 30.1(5) | −0.16(1) |
| Clinac | 6 | 33.8(5) | −0.18(1) |
| | 18 | 36.2(5) | −0.17(1) |
| Mevatron | 6 | 22.3(5) | −0.13(2) |
| | 18 | 22.7(4) | −0.11(1) |

much smaller than those of the other two linacs. Sikora and Alber (2009) for an Elekta Precise operated at 6 MV and 15 MV obtained $\sigma_{\rm ref} = 31.0$ and $k = -0.16$, very close to our values.

In general, the two VSM models provide a similar description of the percentage depth doses both in- and off-axis. This is because both models use the same energy spectra for the initial electrons. However, marked differences appear for the depth profiles in which the single-source model shows sizes that are either wider or narrower (up to about 1 cm more or less in the penumbra) than the "pseudo-data" profiles that are better described by the two-source model. This effect seems to be linked to the electron contamination produced in air. Thus for the low energy configurations (see figure 5), the in-air electron contamination included in the single-source model is that occurring between the flattening filter and the secondary collimators only. However, the contribution of the remaining air gap (up to reach the patient) is relevant and as a consequence the profiles are narrower than those found with our VSM which show an overall agreement with the reference ones. For the high energy configurations (see figure 6) the in-air scattering is relatively less important but the consideration of a restricted air gap makes the model to enhance the source size producing transverse profiles that are wider than those found with PENELOPE and the two-source model proposed here.

In order to go deeper into the capabilities of our VSM, other field configurations have been studied. In figure 7 we show the results obtained when the phantom surface is situated at $z = 115$ cm for the Mevatron at 18 MV (left panels) and the Clinac at 6 MV (right panels). In the first case a 5 cm × 5 cm field has been considered, while in the last one we chose a 10 cm × 10 cm field. In figure 8 the percentage depth doses and transverse profiles obtained for a half beam field of 5 cm × 10 cm in the case of the Mevatron at 6 MV (left panels) and the Precise at 15 MV (right panels).

For the 10 cm × 10 cm field in the Clinac at 6 MV (right panels of figure 7), the VSM provide a description of the MC results that is similar to that found in the previous figures. In the case of the 5 cm × 5 cm field for the Mevatron at 18 MV (left panels in figure 7) and for the half beam field in figure 8, the description of the tails becomes worse, though the peaks of the transverse profiles are rather well reproduced.

This could be ascribed to the method used for determining the direction of emission of the electrons from the respective sources. In the case of the percentage depth doses, some of them are even better described by the two-source model than in the other cases analyzed (see figure 8).

In practice, the commissioning of the present VSM must be carried our together with that of the photon sources. In this sense, both the geometrical and energy distributions of the electron sources may be correlated to those of the photon ones (González 2015). The fluence distributions are then obtained by fitting experimental data obtained from dose measurements in air. The energy distribution can be obtained by using the procedure proposed by Sikora *et al* (2007) in which the calculated percentage depth dose profiles are fitted to the experimental ones. Finally, a fine tuning of the parameters of the source model may be performed by improving the description of the experimental doses measured in the phantom.

As the sources included in the VSM are upstream the secondary collimation system, the simulation of a multileaf collimator may be performed as a standard simulation (with photons and electrons emitted from their corresponding sources) either including the whole MLC geometry (if it is available) or assuming a mathematic collimation of the beams. This has been investigated for an Elekta Precise at 6 MV with a micro-MLC with reasonably good results (González 2015).

## 4. Conclusions

In this work a source model to describe the electron contamination contribution in clinical linacs operating in photon mode has been proposed and evaluated. The model includes two-sources that take into account the electrons produced in the linac head and in the air gap between it and the patient. Six configurations corresponding to three linacs with two qualities each one have been analyzed.

The evaluation of the model has been done in two steps. In the first one, the free parameters of the spatial distributions were obtained by fitting a series of fluences in air at the phantom entrance for various radiation field sizes obtained in a complete MC simulation performed by considering the detailed geometries of the linac heads. In a similar way, the energy spectra for the electrons emitted from the sources were determined from PSF files obtained in these complete simulations.

In the second step, the model was compared to the complete simulation by using the percentage depth doses and transverse dose profiles at various depths in a water phantom. In general, and for the all radiation fields, the results of the calculations performed with the two-source model are in good agreement with those obtained using the whole geometry of the linac head. The largest differences in the percentage depth doses occurred at the entrance of the phantom, for the 6 MV configurations and the 5 cm $\times$ 5 cm radiation fields, reaching $\sim 15\%$ at most.

The VSM profiles have been also compared to those provided by a single-source model with an energy dependent spatial distribution. The single-source model produces

transverse profiles that are up to about 1 cm narrower or wider than the MC ones which, on the contrary, are much better described by our VSM. These results point out that the whole in-air electron contamination must be taken into account to permit an adequate description of the dose absorbed in the water phantom.

## Acknowledgments

We are indebted to Aldo Barreras Cabrera, Manuel Vilches and Lorenzo Brualla for providing us with information concerning the various linac geometries. This work has been partially supported by the Spanish Ministerio de Economía y Competitividad (FPA2009-14091-C02-02, IPT-300000-2010-3, FPA2012-31993), the European Fund for Regional Development (FEDER) and the Junta de Andalucía (FQM-0220, P09-FQM-5431).

## Appendix. Calculation of the fluence contributions

The fluences $\phi_{\rm H}(x,y,z)$ and $\phi_{\rm A}(x,y,z)$ are the contributions of the head and air sources to the total electron fluence, respectively. They can be calculated by integrating conveniently the spatial distribution of the corresponding source, $S_\alpha(x',y')$ (Jiang *et al* 2001, Fippel *et al* 2003):

$$\phi_\alpha(x,y,z) \;=\; \frac{(z_{\rm D}^x - z_\alpha)(z_{\rm D}^y - z_\alpha)}{(z-z_\alpha)^2} \int_{-x_\alpha^-}^{x_\alpha^+}\int_{-y_\alpha^-}^{y_\alpha^+} {\rm d}x'\,{\rm d}y'\,S_\alpha(x',y')\,, \tag{13}$$

where $\alpha = {\rm H,A}$ and $z_\alpha$ indicates the $z$-coordinate of the position of the source: $z_{\rm S}$ and $z_{\rm U}^y$, respectively. The coordinates $z_{\rm D}^x$ and $z_{\rm D}^y$ correspond to the lower ends of the collimation system in the directions $x$ and $y$, respectively. The factor in front of the integral takes into account the reduction of the fluence with the inverse of the square of the distance to the source.

The integration limits $x_\alpha^\pm$ and $y_\alpha^\pm$ in equation (13) delimite the source area seen from $(x,y,z)$, the point at which the fluence is calculated. This area depends on the collimation system of the linac. Let us suppose (see figure 9) the source at $z=z_\alpha$ with the isocenter at $(0,0,z_{\rm I})$. The field size in the $y$-direction is $w_{\rm I}^y = 2Y_{\rm I}$. The upper limit $y_\alpha^+$ in the $y$-integral in equation (13) depends on the the upper or the lower ends of the collimation system (given in table 1 for the various linacs). Thus, if $y < zY_{\rm I}/z_{\rm I}$ (see figure 9),

$$y_\alpha^+ \;=\; \frac{w_{\rm I}^y\, z_{\rm U}^y\,(z-z_\alpha) + 2\,y\,z_{\rm I}\,(z_\alpha - z_{\rm U}^y)}{2z_{\rm I}\,(z-z_{\rm U}^y)}\,, \tag{14}$$

while if $y > zY_{\rm I}/z_{\rm I}$,

$$y_\alpha^+ \;=\; \frac{w_{\rm I}^y\, z_{\rm D}^y\,(z-z_\alpha) + 2\,y\,z_{\rm I}\,(z_\alpha - z_{\rm D}^y)}{2z_{\rm I}\,(z-z_{\rm D}^y)}\,. \tag{15}$$

In a similar way one can determine the lower integration limit $y_\alpha^-$ as well as those in the $x$-direction. Finally one has

$$x_\alpha^\pm = \min\left[\frac{w_\mathrm{I}^x\, z_\mathrm{U}^x\,(z-z_\alpha) \pm 2\,x\,z_\mathrm{I}\,(z_\alpha - z_\mathrm{U}^x)}{2z_\mathrm{I}\,(z-z_\mathrm{U}^x)}, \frac{w_\mathrm{I}^x\, z_\mathrm{D}^x\,(z-z_\alpha) \pm 2\,x\,z_\mathrm{I}\,(z_\alpha - z_\mathrm{D}^x)}{2z_\mathrm{I}\,(z-z_\mathrm{D}^x)}\right] \quad (16)$$

and

$$y_\alpha^\pm = \min\left[\frac{w_\mathrm{I}^y\, z_\mathrm{U}^y\,(z-z_\alpha) \pm 2\,y\,z_\mathrm{I}\,(z_\alpha - z_\mathrm{U}^y)}{2z_\mathrm{I}\,(z-z_\mathrm{U}^y)}, \frac{w_\mathrm{I}^y\, z_\mathrm{D}^y\,(z-z_\alpha) \pm 2\,y\,z_\mathrm{I}\,(z_\alpha - z_\mathrm{D}^y)}{2z_\mathrm{I}\,(z-z_\mathrm{D}^y)}\right] . \quad (17)$$

## References


Ahnesjö A, Saxner M and Trepp A 1992 A pencil beam model for photon dose calculation *Med. Phys.* **19** 263-73

Akaike H 1974 A new look at the statistical model identification *IEEE Transactions on Automatic Control* **19 (6)** 716-23

Chetty I J, Curran B, Cygler J E, DeMarco J J, Ezzell G, Faddegon B A, Kawrakow I, Keall P J, Liu H, Ma C M C, Rogers D W O, Seuntjens J, Sheikh-Bagheri D and Siebers J V 2007 Report of the AAPM Task Group No. 105: Issues associated with clinical implementation of Monte Carlo-based photon and electron external beam treatment planning *Med. Phys.* **34** 4818-53

Ding G X 2002 Energy spectra, angular spread, fluence profiles and dose distributions of 6 and 18 MV photon beams: results of Monte Carlo simulations, for a Varian 2100EX accelerator *Phys. Med. Biol.* **47** 1025-46

Fippel M, Haryanto F, Dohm O, Nüsslin F and Kriesen S 2003 A virtual photon energy fluence model for Monte Carlo dose calculation *Med. Phys.* **30** 301-11

Fix M K, Keall P J and Siebers J V 2005 Photon-beam subsource sensitivity to the initial electron-beam parameters *Med. Phys.* **32** 1164-75

González W, Lallena A M and Alfonso R 2011 Monte Carlo simulation of the dynamic micro-multileaf collimator of a LINAC Elekta Precise using PENELOPE *Phys. Med. Biol.* **56** 3417-31

González W 2015 Modelo de fuentes virtuales para cálculos Monte Carlo en radioterapia externa con haces de fotones Ph. D. Thesis Universidad de Granada

Jia X, Gu X, Jiang Y, Folkerts M and Jiang S B 2011 GPU-based fast Monte Carlo simulation for radiotherapy dose calculation *Phys. Med. Biol.* **56** 7017-31

Korhonen L 2009 Methods for dose calculation and beam characterization in external photon beam radiotherapy Ph. D. Thesis Helsinki University of Technology (available at http://lib.tkk.fi/Diss/2009/isbn9789522481740/isbn9789522481740.pdf)

López-Medina A, Teijeiro A, Garcia J, Esperon J, Terron J A, Ruiz D P and Carrion M C 2005 Characterization of electron contamination in megavoltage photon beams *Med. Phys.* **32** 1281-92

Lee Kuo-Wei, Jian-Kuen W, Jeng Shiu-Chen, Liu Yen-Wan H and Cheng J Chia-Hsien 2009 Skin dose impact from vacuum immobilization device and carbon ber couch in intensity modulated radiation therapy for prostate cancer *Med. Dosim.* **34** 228-32

Press W H, Teukolsky S A, Vetterling W T and Flannery B P 1992 *Numerical recipes in Fortran* 2nd edn (New York: Cambridge University Press)

Rodríguez M, Sempau J and Brualla L 2013 PRIMO. A graphical environment for the Monte Carlo simulation of Varian and Elekta linacs *Strahlenther. Onkol.* **189** 881-6

Salvat F, Fernández-Varea J M and Sempau J 2008 PENELOPE A Code System for Monte Carlo Simulation of Electron and Photon Transport (Paris:NEA)

Sempau J, Wilderman S J and Bielajew A F 2000 DPM, a fast, accurate Monte Carlo code optimized for photon and electron radiotherapy treatment planning dose calculations *Phys. Med. Biol.* **45** 2263-91

Sheikh-Bagheri D and Rogers D W 2002 Sensitivity of megavoltage photon beam Monte Carlo simulations to electron beam and other parameters *Med. Phys.* **29** 379-90

Sikora M and Alber M 2009 A virtual source model of electron contamination of a therapeutic photon beam *Phys. Med. Biol.* **54** 7329-44

Sikora M, Dohm O and Alber M 2007 A virtual photon source model of an Elekta linear accelerator with integrated mini MLC for Monte Carlo based IMRT dose calculation *Phys. Med. Biol.* **52** 4449-63

Yang J, Li J S, Qin L, Xiong W and Ma C-M 2004 Modelling of electron contamination in clinical photon beams for Monte Carlo dose calculation *Phys. Med. Biol.* **49** 2657-73

Ulmer W, Pyyry J and Kaissl W 2005 A 3D photon superposition/convolution algorithm and its foundation on results of Monte Carlo calculations *Phys. Med. Biol.* **50** 1767-90

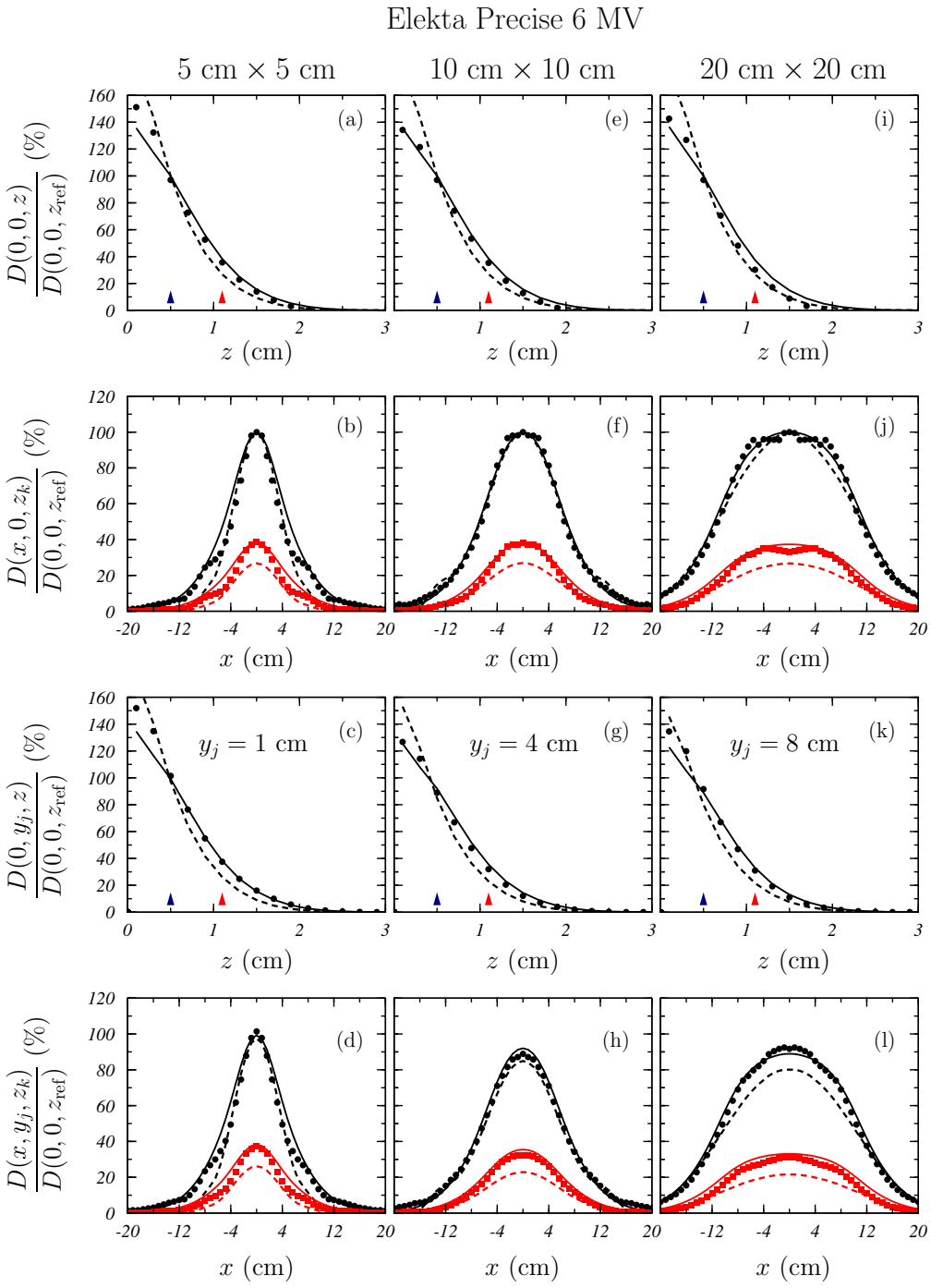


**Figure 5.** Percentage depth doses (panels (a), (c), (e), (g), (i) and (k)) and transverse profiles (panels (b), (d), (f), (h), (j) and (l)) for the 6 MV Elekta Precise linac. Left, central and right panels correspond to the 5 cm × 5 cm, 10 cm × 10 cm and 20 cm × 20 cm radiation fields. Panels (a), (b), (e), (f), (i) and (j) correspond to in-axis profiles, while the remaining panels show off-axis profiles. PENELOPE results obtained with the full geometry are shown with symbols. Solid lines (dashes lines) correspond to the two-source (single-source) model results calculated with DPM. The black and red arrows in panels (a), (c), (e), (g), (i) and (k) indicate the depths $z_k$ at which the corresponding black and red transverse profiles shown in panels (b), (d), (f), (h), (j) and (l) were evaluated. Here $z_{\rm ref} = 0.5\,$cm. The phantom surface is situated at $z = 100\,$cm.

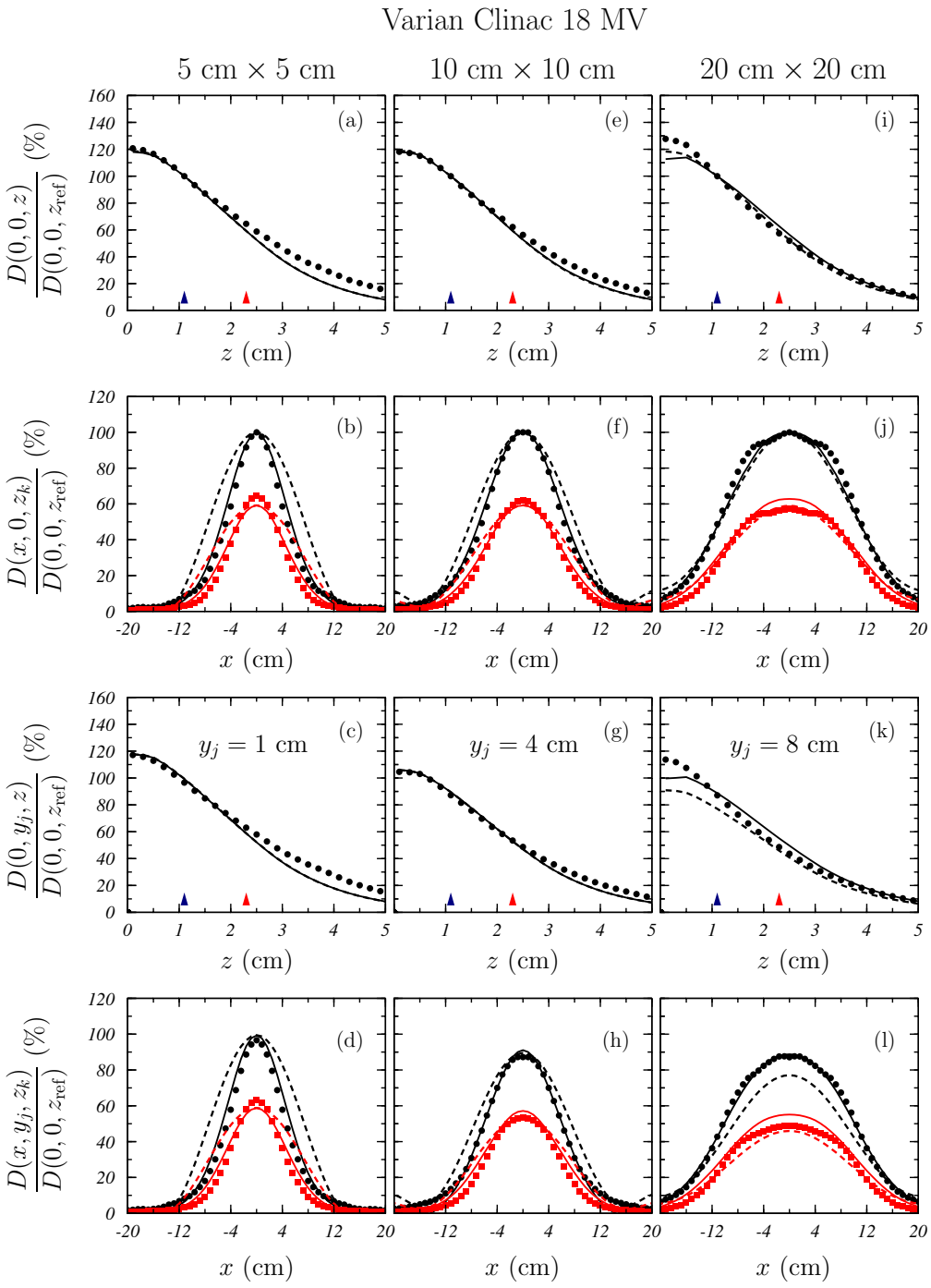


**Figure 6.** Same as in figure 5 but for the 18 MV Varian Clinac linac. Here $z_{\rm ref} = 1.1\,$cm.

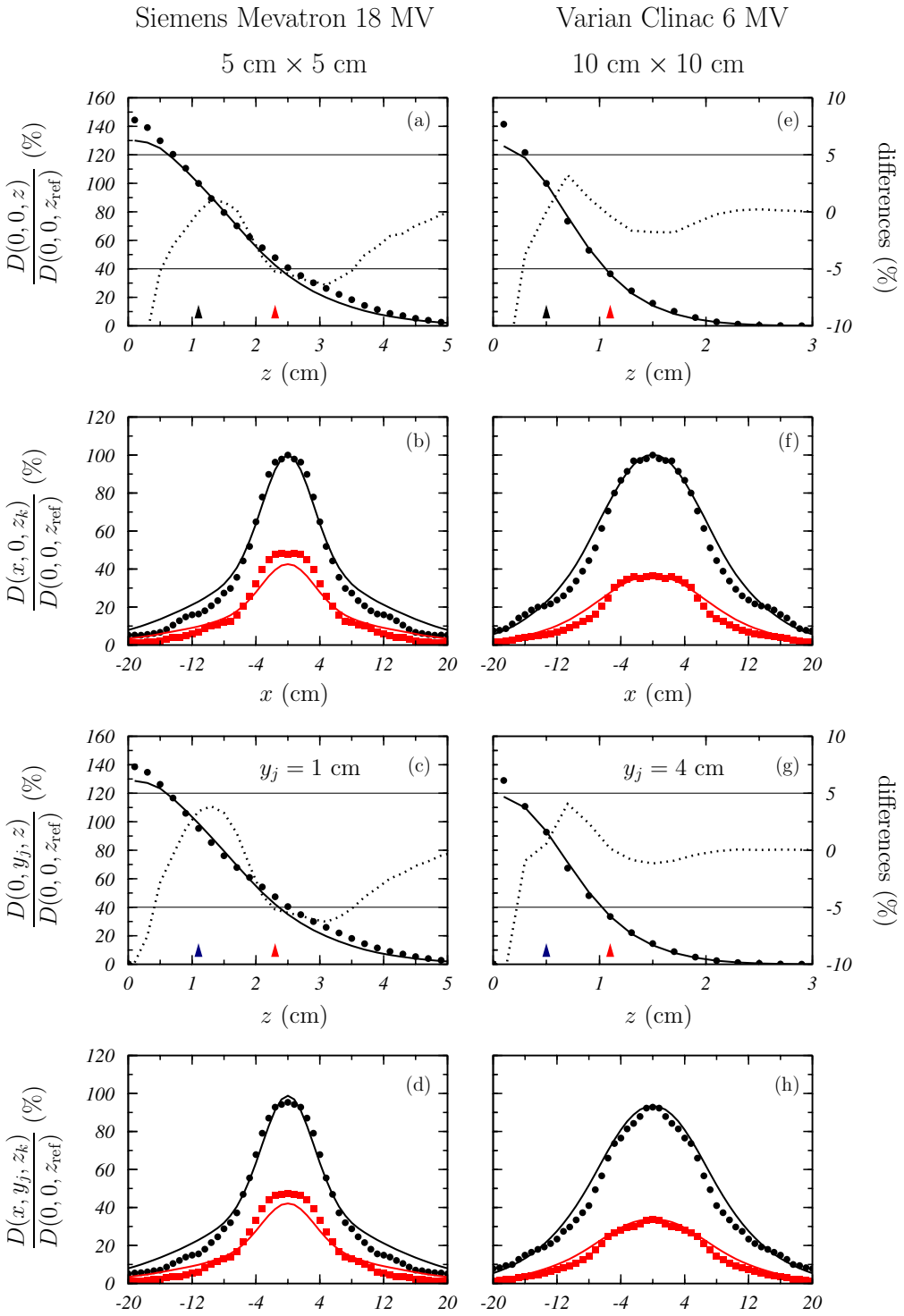


**Figure 7.** Percentage depth doses (panels (a), (c), (e) and (g)) and transverse profiles (panels (b), (d), (f) and (h)) for the 5 cm × 5 cm field in the case of the Mevatron at 18 MV (left panels), $z_{\rm ref} = 1.1\,$cm, and the 10 cm × 10 cm field for the Clinac at 6 MV (right panels), $z_{\rm ref} = 0.5\,$cm. The phantom surface is situated at $z = 115\,$cm. The meaning of the symbols and curves is the same as in figure 5.

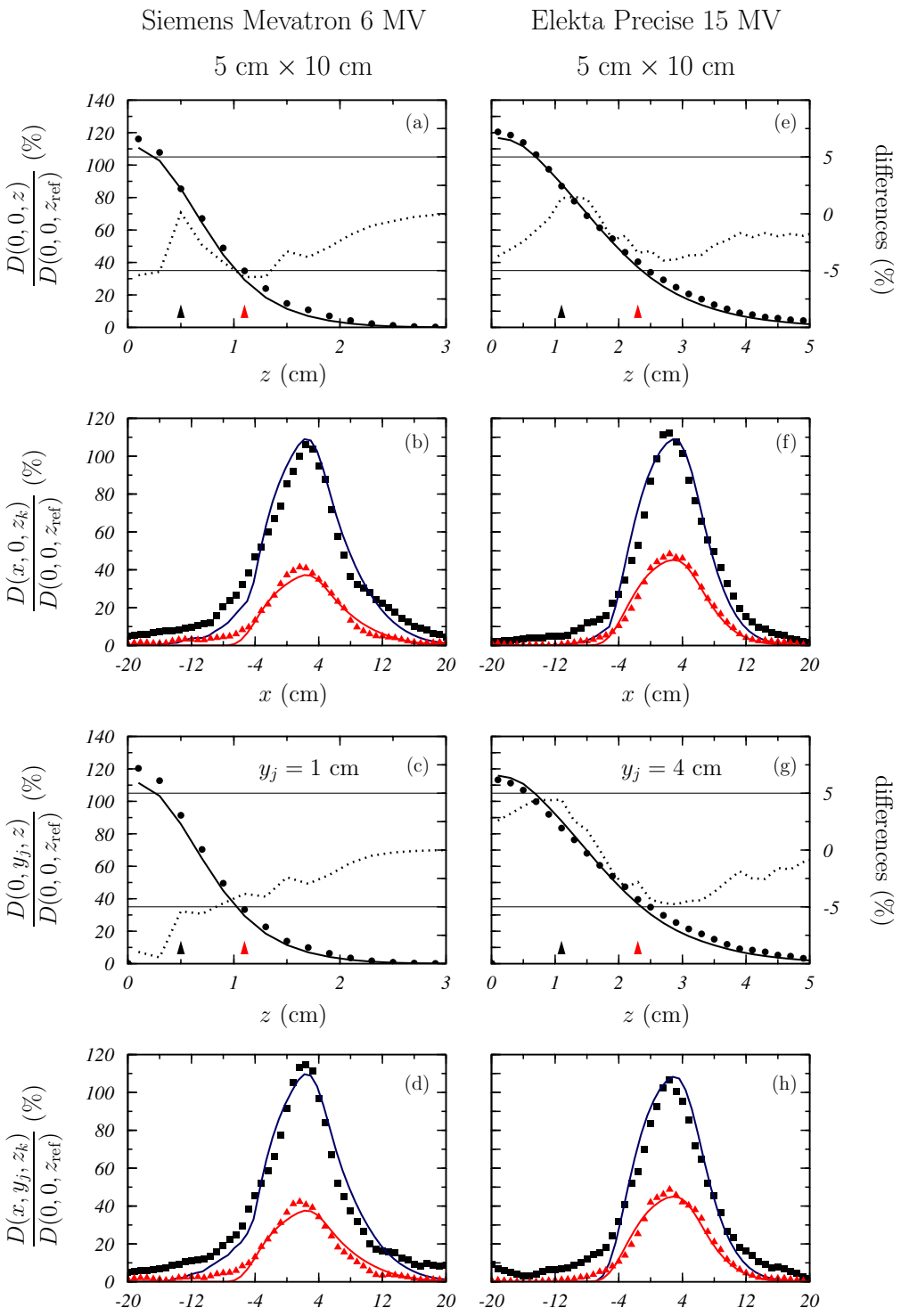


**Figure 8.** Percentage depth doses (panels (a), (c), (e) and (g)) and transverse profiles (panels (b), (d), (f) and (h)) for the 5 cm × 10 cm half-field in the cases of the Mevatron at 6 MV, with $z_{\rm ref} = 0.5$ cm, (left panels) and the Precise at 15 MV, with $z_{\rm ref} = 1.1$ cm, (right panels), $z_{\rm ref} = 0.5$ cm. The phantom surface is situated at $z = 100$ cm. The meaning of the symbols and curves is the same as in figure 5.

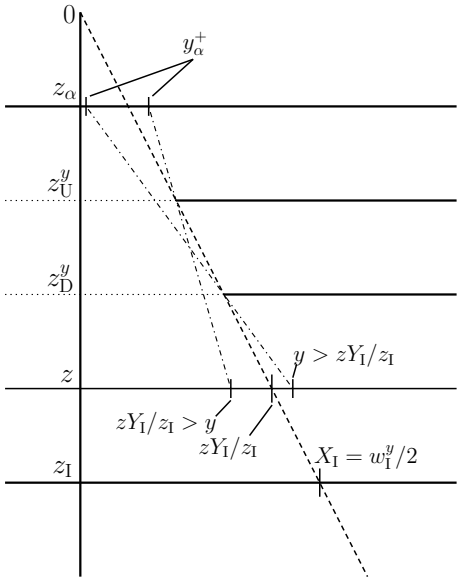


**Figure 9.** Visual field model. The figure illustrates the way how the limits to perform the integration in equation (13) are defined (see text).